International Journal of Greenhouse Gas Control 20 (2014) 324–332

Contents lists available at ScienceDirect

International Journal of Greenhouse Gas Control

journal homepage: www.elsevier.com/locate/ijggc

Engineered CO_2 injection: The use of surfactants for enhanced sweep efficiency

Seunghee Kim [a,*], J. Carlos Santamarina [b,1]

[a] Bureau of Economic Geology, Jackson School of Geosciences, University of Texas at Austin, University Station, Box X, Austin, TX 78713, USA
[b] School of Civil and Environmental Engineering, Georgia Institute of Technology, 790 Atlantic Drive, N.W., Atlanta, GA 30332, USA

ARTICLE INFO

Article history:
Received 5 January 2013
Received in revised form
18 November 2013
Accepted 21 November 2013
Available online 12 December 2013

Keywords:
Carbon dioxide
Interfacial tension
Surfactant
Engineered injection
Sweep efficiency

ABSTRACT

Poor CO_2 displacement efficiency can exacerbate hydro-chemo-mechanically coupled phenomena in CO_2 storage reservoirs, increase the area affected by CO_2 in the reservoir, and negatively impact the long-term geological storage of CO_2. The injection of CO_2 can be engineered using surfactants to improve displacement efficiency. Pendant and sessile drop tests show that a surfonic copolymer decreases the interfacial tension γ_{fl} and increases the contact angle θ under reservoir conditions. The combined changes in surface tension and contact angle have a pronounced effect on the capillary factor $\gamma_{fl}\cdot\cos\theta$. Injection tests using micro-models and pore network simulations show that a smaller capillary factor transforms the displacement pattern and enhances the pore-scale sweep efficiency of CO_2, surpassing 40% in 2-D applications. Surfactant cost may offset the technical advantages identified in this study.

1. Introduction

Fossil fuels account for ~85% of all energy consumption and result in 30 Gt of CO_2 emissions per year worldwide (Tsouris et al., 2010). Our dependency on fossil fuels will continue for the coming decades, until alternative energy sources can satisfy both current and anticipated demands (EIA, 2010; Pasten and Santamarina, 2012). Meanwhile, carbon capture and storage may allow for a more sustainable use of fossil fuels (Baines and Worden, 2004; Dooley et al., 2006).

Geological formations that are candidates for CO_2 geological storage include depleted hydrocarbon reservoirs, oil reservoirs (as part of enhanced oil recovery), unminable coal seams, salt caverns, and deep saline aquifers (IPCC, 2005). The use of depleted hydrocarbon reservoirs and salt caverns for CO_2 storage competes with natural gas storage, and does not necessarily match the geographic distribution of CO_2 sources (EIA, 2004; Pusch et al., 2010). Deep saline aquifers are most promising because of their large storage capacities (~10^3 and 10^4 $GtCO_2$), and their advantageous proximity to stationary CO_2 emission sources such as coal power plants in the USA (IPCC, 2005).

High storage efficiency can develop in geologic traps where upward buoyant migration controls occupancy (Bryant et al., 2008). On the other hand, the CO_2 storage capacity G_{CO_2} [Gt] in reservoirs with horizontal, zero-dip seal-rocks is determined by the storage efficiency E [–] which can be between $E = 0.005$ and 0.055 (NETL, 2010; Okwen et al., 2010). The storage capacity G_{CO_2} for a reservoir with areal extent A_t [km^2], mean pool thickness H_{CO_2} (which is determined by capillarity so that $H_{CO_2} \leq H_R$ where H_R is the thickness of the reservoir layer), porosity φ [–], and CO_2 density ρ_{CO_2} [kg/m^3] is $G_{CO_2} = E \cdot \varphi \cdot A_t \cdot H_{CO_2} \cdot \rho_{CO_2}$. Let us consider a target sequestration of $G_{CO_2} = 750$ $GtCO_2$ over the next 50 years in the world (15 $GtCO_2$/year – Espinoza et al., 2011) under supercritical conditions (density $\rho_{CO_2} = 600$ kg/m^3) in typical reservoirs (pool thickness $H_{CO_2} = 10$ m, porosity $\varphi = 0.2$, high storage efficiency factor $E = 0.055$); the estimated storage area will affect ~1,000,000 km^2, which is similar to the area of Texas or France.

A large areal extent increases the probability of leaks along intersecting faults and abandoned wells, hydro-chemo-mechanical coupled effects, fault reactivation, and induced seismicity. In addition, monitoring strategies will have to cover large areas, and compensation will extend to a large number of property owners (Gresham et al., 2010). The purpose of this study is to explore alternatives to engineer the injection of CO_2 in order to improve sweep efficiency E in deep saline reservoirs. Relevant processes are reviewed first.

* Corresponding author. Tel.: +1 404 805 3724; fax: +1 512 471 0140.
E-mail addresses: simseung@gmail.com, seunghee.kim@beg.utexas.edu (S. Kim), jcs@gatech.edu (J.C. Santamarina).
[1] Tel.: +1 404 894 7605; fax: +1 404 894 2281.

1750-5836/$ – see front matter © 2013 Elsevier Ltd. All rights reserved.
http://dx.doi.org/10.1016/j.ijggc.2013.11.018

2. Processes relevant to engineered CO_2 injection

2.1. Increased CO_2 viscosity and foams

More homogeneous displacement patterns in CO_2-enhanced oil recovery have been achieved using (1) thickening agents such as polymers (Alvarado and Manrique, 2010; Enick et al., 2010; Enick and Olson, 2012; Huh and Rossen, 2008) and (2) emulsification/foams employing surfactants (Enick and Olson, 2012; Kam and Rossen, 2003; Kovscek and Bertin, 2003; Levitt et al., 2009). In particular, foams enhance sweep efficiency by preferentially blocking the larger flow channels forcing CO_2 migration into smaller pores (Enick and Ammer, 1998; Farajzadeh et al., 2009; Kovscek and Bertin, 2003). These strategies can increase oil recovery by as much as 80% (Lake and Venuto, 1990; Levitt et al., 2009).

2.2. Sequential fluid injection

Viscous fingering is lessened and CO_2 displacement is enhanced by the intermediate injection of a fluid with density, viscosity, and wetting properties that are between the properties of brine and CO_2 (Alvarado and Manrique, 2010). Furthermore, the intermediate fluid can be miscible in both brine and CO_2. Acetone is an example of the intermediate fluid (viscosity $\approx$ 0.3 mPa s at T = 30 °C and P = 0.1 MPa, density $\approx$ 780 kg/m^3 at T = 35 °C and P = 0.1 MPa – Kinart et al., 2002), and it is miscible with both water and CO_2 (Liu and Kiran, 2007; Pečar and Doleček, 2005; Tanaka et al., 1987). A properly selected/engineered intermediate fluid injected prior-to or simultaneously with CO_2 alters the fluid displacement pattern and improve storage efficiency.

2.3. Bio-clogging

Microbial activity can be stimulated in water-filled flow paths (Bryant and Britton, 2008; Phillips et al., 2012) as long as pores exceed a nominal size $d_{pore} \sim 1\,\mu m$ (Phadnis and Santamarina, 2011; Rebata-Landa and Santamarina, 2006). Preferential bio-clogging of the larger water-filled pores will cause flow to divert to low-permeability channels. Compiled results suggest that bio-clogging will be most effective in sediments with permeability 10 md $\leq k \leq$ 10 Darcy (Rebata-Landa and Santamarina, 2012).

2.4. Modifying the capillary factor

The high CO_2–H_2O interfacial tension γ_{fl} hinders CO_2 invasion into small pores, and contributes to residual water saturation (Chalbaud et al., 2009; Suekane et al., 2005). The interface can be altered by actively imposing electromagnetic fields (Francisca et al., 2008). Yet, the most obvious strategy is to modify the CO_2–H_2O interfacial tension using surfactants such as pluronic block copolymers, PDMS-g-PEO-PPO copolymers, PEPE, PFPE, ethoxylated acetylenic surfactants, and methylated branched hydrocarbon surfactants (da Rocha et al., 1999; Dickson et al., 2005; Ryoo et al., 2003; Stone et al., 2004). The anticipated change in surface tension γ as a function of surfactant concentration C_s [mol/m^3] and surface excess concentration Γ [mol/m^2] is captured in the Gibbs adsorption equation (Dickson et al., 2005):

$$\frac{d\gamma}{d\log C_s} = -\Gamma RT \quad (1)$$

where R = 8.314 J/mol/K is the gas constant. Surfactants may change the water-mineral interfacial tension γ_{fl} and the contact angle θ against mineral surfaces. Both effects are depicted in the capillary factor $\gamma_{fl}\cdot\cos\theta$. The use of surfactants and implications on the capillary factor are explored next.

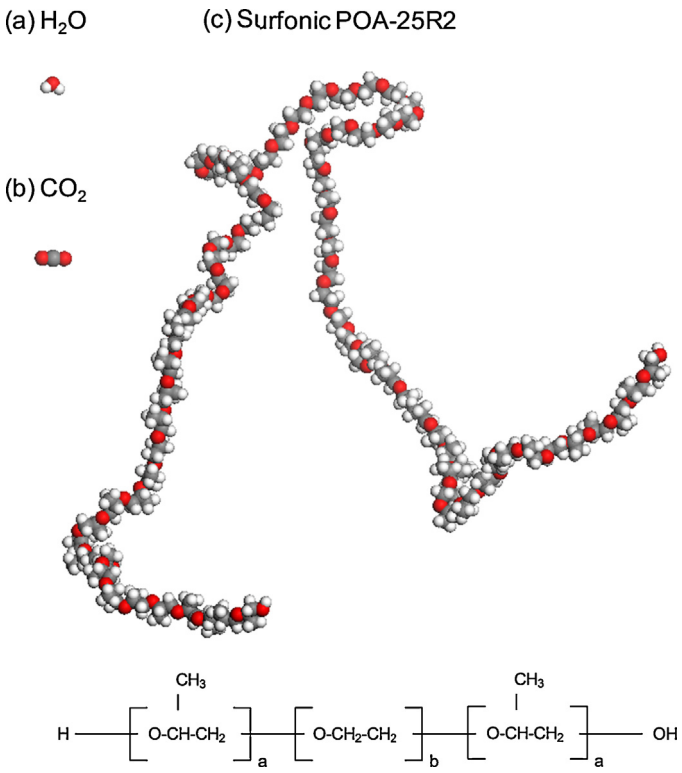

Fig. 1. Molecular structure of: (a) H_2O, (b) CO_2, and (c) surfonic POA-25R2. This surfactant consists of a central hydrophilic chain of polyoxyethylene and two flanked hydrophobic chains of polyoxypropylene (a = 22 and b = 38 in the diagram). The molecular structure is inspired from Kozlov et al. (2000) and Prasad et al. (1979), and its visualization is courtesy of Q. Zhao.

3. Engineered injection by capillary factor control – experimental study

The modification of the capillary factor and its implications are explored herein. First, we measure the water–CO_2 interfacial tension and contact angle as a function of pressure, with and without surfactants. Then we conduct fluid displacement experiments within a porous micro-model.

3.1. Surface tension and contact angle

3.1.1. Surfactant

The surfactant selected for this study is SURFONIC POA-25R2 (HUNTSMAN), which is a reversed block copolymer composed of hydrophilic polyoxyethylene and CO_2-philic polyoxypropylene (Fig. 1). Published results suggest that this surfactant can lower the CO_2–water interfacial tension to ~3 mN/m at a ~0.1% volumetric concentration of surfactant (temperature T = 45 °C, and pressure P = 27 MPa – da Rocha et al., 1999). This surfactant is a water soluble, nonionic surface active agent, and has the hydrophilic/lipophilic balance HLB = 6.3 (Note: a value HLB = 7 denotes even partitioning of surfactants between two phases). The nonionic surfactant molecules diffuse in water, adsorb at the CO_2–H_2O interface, and change the local electric field as they partition between the two phases (De Gennes et al., 2004).

3.1.2. Test procedure

This study uses the high pressure chamber shown in Fig. 2a (details in Espinoza and Santamarina, 2010). The chamber is first subjected to three cycles of vacuum and CO_2 flushing (99.99% purity) to remove air. At a CO_2 pressure $P \approx$ 0.1 MPa, water or water mixed with surfactant is injected using a high-pressure syringe to

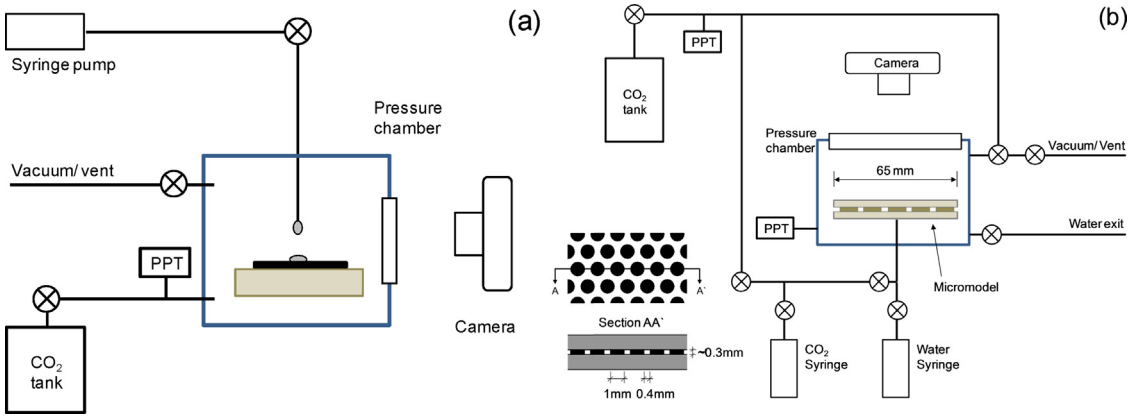

Fig. 2. Experimental devices. (a) High pressure chamber for the measurement of interfacial tension γ_{fl} and contact angle θ. (b) CO_2 injection test using a micro-model housed in a high pressure chamber. *Note*: PPT, pore pressure transducer.

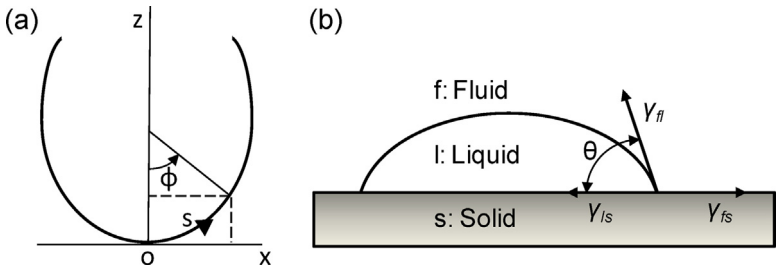

Fig. 3. Surface tension and contact angle. (a) Coordinate system for pendant drop analysis. (b) Contact angle formed by a liquid droplet *l* surrounded by fluid *f*, sitting on substrate *s*.

form a droplet that hangs at the tip of a stainless steel needle and/or a sessile droplet that sits on a SiO_2 glass substrate (Note: surfactant concentration $wt = 0.4\%$; for reference, the critical micelle concentration is $wt = 1\%$ at $T = 28$–$32\,^{\circ}C$; deionized and degased water is used). Thereafter, the chamber is pressurized with CO_2 in steps, from the initial 0.1 MPa pressure to 10 MPa. A high-resolution camera captures the shape of the droplet through a sapphire window (Fig. 2a).

3.1.3. Data reduction

Recorded images are analyzed using Laplace's equation in parametric form to determine interfacial tension γ_{fl} and contact angle θ (Rotenberg et al., 1983):

$$\gamma_{fl}\left(\frac{d\phi}{ds}+\frac{\sin\phi}{x}\right)=\frac{2\gamma_{fl}}{R_0}+\Delta\rho g z \qquad (2)$$

where R_0 [m] denotes the radius at the droplet apex, (x, z) are the cartesian coordinates from the droplet apex, (s, ϕ) are the coordinates along the arc length (Fig. 3a). The density difference $\Delta\rho$ [kg/m^3] between CO_2 and water is computed as a function of pressure and temperature using equations in Duan and Sun (2003). The inverted interfacial tension γ_{fl} and contact angle θ are the values that minimize the square error between the theoretical droplet shape and the experimentally captured image.

3.1.4. Surface tension

Error surfaces as a function of the interfacial tension γ_{fl} and the curvature at the apex R_0 are convex as shown in Fig. 4. Results in Fig. 4 also show that the sensitivity in the determination of the interfacial tension γ_{fl} is in the order of ± 0.2 mN/m. The effect of the surfactant on surface tension is readily seen in the shape of the pendant drop (Fig. 5a). The addition of surfactant decreases the CO_2–water interfacial tension from ~50 mN/m (at 0.1 MPa) to a stable value of ~4 mN/m when P–T conditions reach the liquid–gas boundary (Fig. 5b). The trend parallels the interfacial tension for CO_2–water, with an almost constant shift of 25–35 mN/m. Note that the pendant drop test is not affected by the interfacial tension between water and solid γ_{ls}, and between CO_2 and solid γ_{fs} (Fig. 3b).

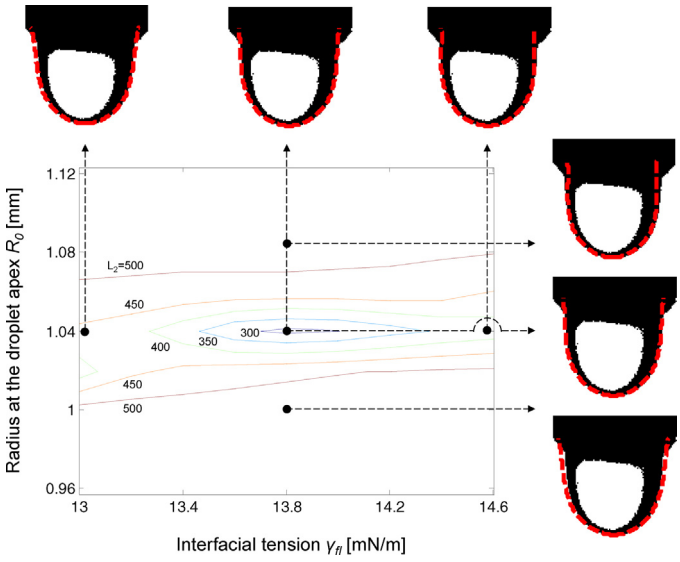

Fig. 4. Sensitivity analysis. Error surfaces as a function of interfacial tension γ_{fl} and the curvature radius at the apex of a pendant drop R_0. Images show both the theoretical shape of the pendant drop and the photographed shape (pressure $P = 5.4$ MPa, temperature $T = 25\,^{\circ}C$, density of water $\rho_{water} \approx 998.4$ kg/m^3, and density of CO_2 $\rho_{CO_2} \approx 154.6$ kg/m^3; the density of CO_2 is calculated using equations in Duan and Sun, 2003).

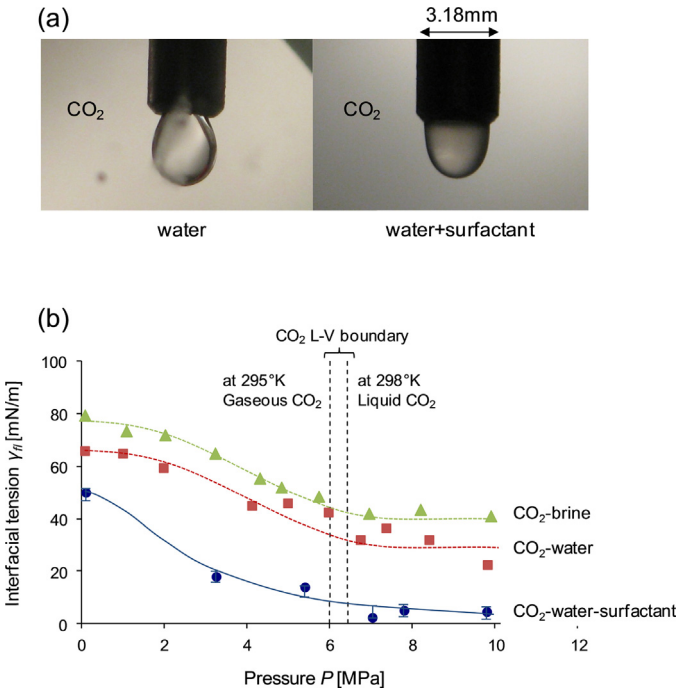

Fig. 5. The effect of surfactant and pressure on interfacial tension γ_{fl}. (a) Images: pendant droplets of water (left, $P = 5.79$ MPa, and $T = 24.5\,^{\circ}$C) and water + surfactant (POA-25R2; $wt = 0.4\%$; right, $P = 5.4$ MPa, and $T = 25\,^{\circ}$C). (b) Fluid pressure effect on interfacial tension: triangle = brine, square = water (from Espinoza and Santamarina (2010) – based on sessile drop measurements), and circle = water + surfactant; POA-25R2, $wt = 0.4\%$.

3.1.5. Contact angle

Images of sessile droplets sitting on the glass substrate reveal the change in contact angle θ with pressure in the presence of the surfactant (Fig. 6). While the contact angle in CO_2–H_2O–SiO_2 remains almost constant as pressure increases (Espinoza and Santamarina, 2010), the contact angle increases from $\theta \sim 20^{\circ}$ at $P = 0.1$ MPa to $\theta \sim 70^{\circ}$ at $P \sim 10$ MPa when the surfactant is present (Fig. 6). Therefore, the capillary factor in the presence of the surfactant $\gamma_{fl}\cdot\cos\theta$ will experience a pronounced decrease as pressure increases.

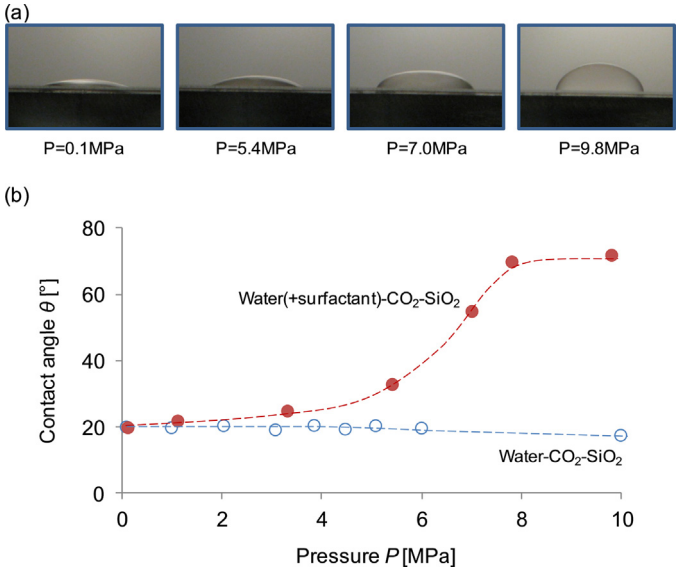

Fig. 6. The effect of surfactant and CO_2 pressure on contact angle θ. (a) Sessile droplets of water + surfactant (POA-25R2; $wt = 0.4\%$) on a glass substrate at various pressure levels ($T = 25\,^{\circ}$C). (b) Variation of contact angle θ with pressure. *Note*: Empty circles are from Espinoza and Santamarina (2010).

3.2. Water displacement by CO_2 injection in a pore micro-model

3.2.1. Test procedure

We conducted water displacement studies by injecting CO_2 into a water-saturated pore micro-model housed inside a high pressure chamber (Note: the device described in Jang (2011) was modified for this study to allow for separate water and CO_2 injections – Fig. 2b). The micro-model (circular plate – diameter $d_{plate} = 65$ mm) was prepared through photo-fabrication and glass etching processes to create a regular pattern of 0.3 mm high cylindrical glass pillars and a porous network with 0.4 mm pore size; a flat glass plate is glued above (cured, aged, and flushed cyanoacrylate). The nominal pore size in the micro-model is $d_{pore} = 0.4$ mm (Fig. 2b). The test procedure involves five steps: (1) all air is evacuated by three cycles of vacuum followed by CO_2 flushing (CO_2 pressure $P = 0.1$–0.2 MPa and temperature $T \sim 25\,^{\circ}$C – 99.99% purity); (2) the micro-model is filled with water (or water with surfactant) while the chamber is under vacuum; (3) the chamber is pressurized with CO_2 through a chamber-dedicated port to a CO_2 pressure $P_{CO_2} \sim 7$ MPa (CO_2 in the liquid state); CO_2 bubbles trapped inside the micro-model contract during pressurization and dissolve in the water; (4) While maintaining the target CO_2 pressure in the chamber at $P \sim 7$ MPa, we inject water (or water with surfactant) through the central port in the micro-model using a high-pressure syringe in volume-control mode to attain complete water saturation in the micro-model; finally, (5) we inject CO_2 through the central port in the micro-model while the chamber pressure is maintained at $P \sim 7$ MPa. The 8 ml of CO_2 stored in the syringe is injected at a rate that varies between 4 and 8 ml/min; eventually, CO_2 percolates through the micro-model peripheral free-draining boundary. A high resolution camera captures CO_2 invasion patterns.

3.2.2. Results

Images shown in Fig. 7 were captured at four different test conditions: water displaced by gaseous CO_2 at $P \sim 0.1$ MPa (a) without and (b) with surfactants, and water displaced by liquid CO_2 at $P \sim 7$ MPa (c) without and (d) with surfactants. Menisci at CO_2–water interfaces within the micro-model confirm that the capillary factor $\gamma_{fl}\cdot\cos\theta$ decreases either as the fluid pressure increases or in the presence of the surfactant, in agreement with change in interfacial tension and contact angle reported in Figs. 5 and 6.

The sweep efficiency E in this 2-D porous network is estimated as the ratio between the area occupied by CO_2 and the area of the entire micro-model. Fig. 8 shows the measured sweep efficiencies as a function of the capillary factor $\gamma_{fl}\cdot\cos\theta$. At a low pressure ($P \sim 0.1$ MPa and $\gamma_{fl}\cdot\cos\theta \sim 68$ mN/m), gaseous CO_2 fingers through the micro-model displacing water in a very small area so that the measured efficiency is $E < 0.1$. The other extreme corresponds to water with surfactant and at high pressure ($P \sim 7$ MPa and $\gamma_{fl}\cdot\cos\theta \sim 3$ mN/m); results show that liquid CO_2 displaces water evenly until it eventually breaks through the model perimeter resulting in a sweep efficiency that surpasses $E > 40\%$. The pore-scale sweep efficiency roughly doubles when the surfactant is added, or when liquid and gaseous CO_2 injections are compared.

4. Numerical study – pore network model

We run network model simulations to further investigate the effect of capillary factor control on CO_2 displacement patterns and sweep efficiency trends. The network simulation algorithm was developed for the case of immiscible drainage where a non-wetting

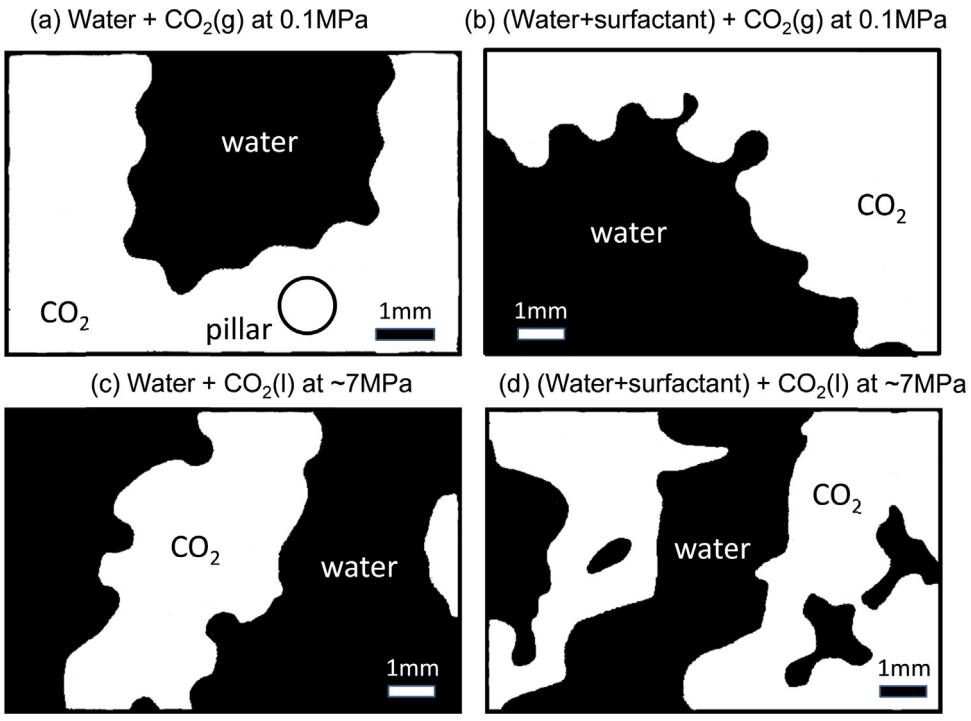

Fig. 7. The interface of a CO_2–water system when CO_2 invades the micro-model that is initially saturated with water (or water + surfactant). The corresponding dimensionless ratios are: $M = \mu_{CO_2}/\mu_w$, and $C = q\mu_{CO_2}/(\gamma_{fl} \cdot \cos\theta)$. (a) $\log M \approx -2.0$, $\log C \approx -8.0$, (b) $\log M \approx -1.3$, $\log C \approx -7.0$, (c) $\log M \approx -1.1$, $\log C \approx -6.5$, and (d) $\log M \approx -0.4$, $\log C \approx -3.8$. *Note*: temperature is $T \sim 25\,^{\circ}C$ for all conditions.

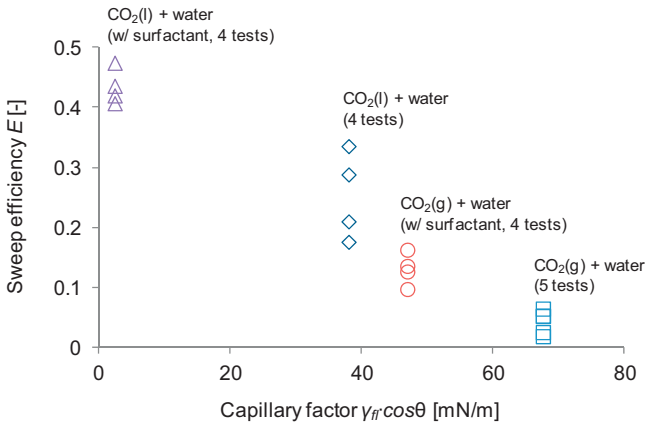

Fig. 8. Experimental results: sweep efficiency E as a function of the capillary factor $\gamma_{fl}\cdot\cos\theta$.

fluid is injected into a medium saturated with a wetting fluid (Aker et al., 1998; Ferer et al., 2003; Lenormand et al., 1988).

4.1. Network construction

The 2-D square network model consists of tubes that intersect at nodes. Tube diameters d are log-normally distributed with mean value $d_0 = 20\,\mu m$ and coefficient of variation COV = 0.4. All tubes have identical length $L_{ch} = 200\,\mu m$. Periodic boundary conditions are imposed on boundaries transverse to the flow direction (Fenwick and Blunt, 1998; Jang, 2011). The network is filled with water at the beginning of the simulation.

4.2. Initial condition

A pressure difference between the inlet and the outlet ΔP_{tot} [Pa] is imposed to determine initial nodal pressures under the water-saturated condition. Nodal fluid pressures are computed by writing the continuity equation at all nodes and solving the system of equations (details in Jang, 2011):

$$q_a + q_b + q_l + q_r = 0 \tag{3}$$

where subindices denote a: above, b: below, l: left, and r: right. The pressure difference ΔP between two adjacent nodes is then used to compute the initial flow velocity v_0 [m/s] and flow rate q_0 [m^3/s] for each tube using Poiseuille's law as a function of the tube diameter d [m], length L_{ch} [m], and the fluid viscosity μ [Pa s]:

$$\text{Initial velocity}: \quad v_0 = \frac{\Delta P d^2}{32\mu L_{ch}} \tag{4}$$

$$\text{Initial flow rate}: \quad q_0 = \alpha_w \cdot \Delta P \tag{5}$$

$$\text{Initial conductance}: \quad \alpha_w = \frac{\pi d^4}{128\mu L_{ch}} \tag{6}$$

where α_w denotes the initial conductance of a tube that is filled with water. The water-saturated flow rate q_{tot} is obtained by summing all flow rates for tubes in the first layer.

4.3. CO_2 invasion

The non-wetting CO_2 is injected at the inlet with the same constant flow rate q_{tot} computed for the water saturated network (under the imposed ΔP_{tot}). We assume that both water and CO_2 are incompressible.

The non-wetting CO_2 invades a tube only if the pressure difference between the two fluids $P_{CO_2} - P_w$ exceeds the tube's capillary pressure $P_c = 4\cdot(\gamma_{fl}\cdot\cos\theta)/d$. As CO_2 displaces water, the pressure drop along the tube reflects CO_2 and H_2O viscous drag and capillary pressure. The flow rate q through the tube is computed based on Poiseuille's law and the total pressure drop from node $i-1$ to node i:

$$q = \alpha_{eff}({P_{CO_2}}^{i-1} - {P_w}^{i} - P_c)|_+ \tag{7}$$

Effective conductance $\alpha_{eff} = \dfrac{\pi d^4}{128 \mu_{eff} L_{ch}}$ (8)

The effective viscosity μ_{eff} is the average of the two viscosities weighted by the length fraction of each fluid in the tube (Lenormand et al., 1988). The positive sign in Eq. (7) denotes a positive value, in other words, the flow rate is $q = 0$ if the pressure difference between the two fluids ${P_{CO_2}}^{i-1} - {P_w}^i$ is smaller than the tube's capillary pressure ${P_{CO_2}}^{i-1} - {P_w}^i < P_c$.

4.4. Nodal pressure

The pressure field in the network model is updated based on mass conservation. Similar to Eqs. (3)–(6), the pressure P_c at a central node in the 2-D porous network is (Ferer et al., 2003):

$$(\alpha^a_{eff} + \alpha^b_{eff} + \alpha^l_{eff} + \alpha^r_{eff})P_c = (\alpha^a_{eff}P_a + \alpha^b_{eff}P_b + \alpha^l_{eff}P_l + \alpha^r_{eff}P_r) + (f^a\alpha^a_{eff}P_c + f^b\alpha^b_{eff}P_c + f^l\alpha^l_{eff}P_c + f^r\alpha^r_{eff}P_c) \quad (9)$$

The f-factor is $f = 1$ if there is a meniscus within the tube, or $f = 0$ otherwise. The system of equations is iteratively solved by simultaneously updating the position of menisci within tubes until equilibrium is reached.

4.5. Invasion

The evolution of invasion is computed using a two-step algorithm. First, fluids advance in each tube for a pre-selected time interval Δt with the velocity computed with the known nodal pressures. The time interval Δt is small so that no meniscus advances more than 10% of the tube length $\Delta t \le 0.1 L_{ch}/v_{max}$. Second, nodal pressures are recomputed for the given inlet and outlet nodal pressures that maintain the flow rate condition constant. We repeat each Δt-cycle until CO_2 reaches outlet nodes (see also Ferer et al., 2003).

4.6. Results

We run multiple random network realizations and simulations for capillary factors $\gamma_{fl}\cdot\cos\theta$=35 mN/m, 5 mN/m, and 1 mN/m to compare the effect of capillarity $\gamma_{fl}\cdot\cos\theta$ on sweep efficiency E. Results show that CO_2 invades more evenly and the sweep efficiency E increases as the capillary factor decreases (Fig. 9). The CO_2 invasion pattern is localized along the larger tubes for a high capillary factor, and changes to a more homogeneous pattern of stable displacement when the capillarity factor is low $\gamma_{fl}\cdot\cos\theta \le 5$ mN/m, all other parameters being constant.

4.7. Note

Experimental and numerical sweep efficiencies reported above are based on 2-D systems. As the pore coordination number increases in 3-D so do the degrees of freedom during invasion, and decreased 3-D sweep efficiencies are anticipated.

5. Analyses and discussion

5.1. Surfactant, pressure, and interfacial tension

The interfacial tension between CO_2 and water decreases from ~70 mN/m to ~30 mN/m as the fluid pressure increases, and reaches a constant value ~30 mN/m beyond the CO_2 gas–liquid boundary (studies at 278–373 K and up to ~70 MPa can be found in: Chun and Wilkinson, 1995; Dickson et al., 2006; Espinoza and Santamarina, 2010; Kvamme et al., 2007; Massoudi and King, 1975; Sutjiadi-Sia et al., 2007). As pressure increases, the CO_2 gas densifies and the concentration of CO_2 near the CO_2–water interface increases, causing the interfacial tension to decrease (Chun and Wilkinson, 1995; Espinoza and Santamarina, 2010; Massoudi and King, 1975). Surfactant molecules align at the CO_2–water interface (Prasad et al., 1979), modify the local electric field at the molecular scale, and weaken the surface tension by adding repulsion forces between molecules near the interface.

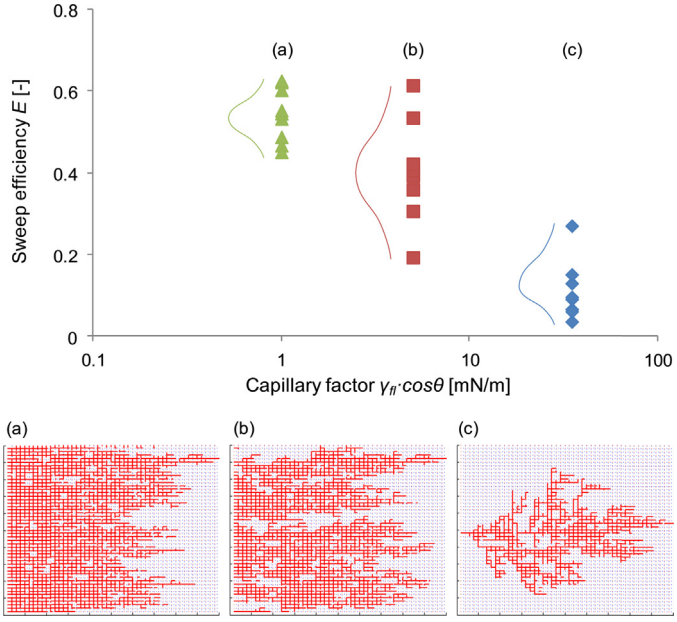

Fig. 9. Network simulations. CO_2 invasion pattern and sweep efficiency for different capillary factors $\gamma_{fl}\cdot\cos\theta$ (10 network realizations were simulated for each capillary factor). *Note*: 50×50 pore network model, average diameter of tubes $d_0 = 20$ μm, length of each tube $L_{ch} = 200$ μm, the coefficient of variation of tube diameters $COV = 0.4$, the viscosity of water $\mu_w = 10^{-3}$ Pa s, the viscosity of CO_2 $\mu_{CO_2} = 5 \times 10^{-4}$ Pa s, the density of water $\rho_w = 1000$ kg/m^3, initial pressure difference between the inlet and the outlet $\Delta P_{tot} = 200$ kPa, and constant flow rate $q_{tot} = 2.8$ mm^3/s.

The Young–Dupre equation relates the contact angle to interfacial tensions (Fig. 3b):

$$\cos\theta = \frac{\gamma_{fs} - \gamma_{ls}}{\gamma_{fl}} \quad (10)$$

Therefore, the capillary factor $\gamma_{fl}\cdot\cos\theta = \gamma_{fs} - \gamma_{ls}$ is a function of the CO_2–mineral γ_{fs} and water-mineral γ_{ls} interfacial tensions. Changes in the capillary factor with pressure and with the addition of surfactants indicate that either γ_{fs} or γ_{ls} changes as well. Indeed, published results show that the interfacial tension γ_{fs} between CO_2 and solid mineral decreases as CO_2 pressure increases from 0.1 MPa to ~7 MPa (Dickson et al., 2006; Sutjiadi-Sia et al., 2008). On the other hand, while the water-mineral interfacial tension γ_{ls} remains relatively constant as the fluid pressure increases (Dickson et al., 2006; Espinoza and Santamarina, 2010), the value of γ_{ls} increases as the concentration of surfactant increases possibly due to hydrogen bonding between the hydro-phobic tail and SiO_2 (Szymczyk and Jańczuk, 2008). Thus, the capillary factor $\gamma_{fl}\cdot\cos\theta$ effectively decreases as the CO_2–water interfacial tension γ_{fl} decreases.

Surfactant sorption to mineral surfaces in the storage reservoir gradually decreases the concentration of surfactants at the CO_2–water interface. Nonionic surfactants such as the one used in this study exhibit reduced adsorption losses (Enick and Olson, 2012). Still, surfactant cost, aggravated by sorptive losses, can offset the technical advantages of enhanced sweep efficiency. While there are commercially available inexpensive surfactants, it is anticipated

that active research currently taking place in this field will lead to improved and more economical CO_2-soluble nonionic surfactants.

We note that the selected pluronic block copolymer surfactant has a molecular weight $mw = 4224$ g/mol and an estimated molecular size of ~20 nm (Fig. 1). The two hydro phobic tails repel each other to form a V-shaped string at the interface. The resulting "wedge" resists invading pores $d_{pore} < 10$ nm. The fraction of pores $d_{pore} < 1$ nm is very small in most shales (<1% – Bachu and Bennion, 2008).

5.2. Implications to CO_2 geological storage

The impact of engineered CO_2 injection extends well beyond efficient volumetric brine displacement. Indeed, poor sweep efficiency implies high residual water saturation and a large water–CO_2 interface; both effects favor hydro-chemo-mechanically coupled interactions in the reservoir that may severely hinder its long-term performance.

Injected CO_2 dissolves into brine and decreases pH. In turn, acidified water prompts mineral dissolution (Kharaka et al., 2006). Extensive experimental evidence, discrete element simulations, and network model simulations show that mineral dissolution can cause: (1) a pronounced decrease in lateral stresses so that the sediment reaches failure under zero lateral strain and shear planes develop (Cha, 2012; Shin and Santamarina, 2009; Shin et al., 2010), (2) localized reactive fluid transport and internal piping (Fredd and Fogler, 1998), (3) skin erosion below the caprock and differential settlement of the caprock that may lead to bending failures and open mode discontinuities (Kim, 2012). Eventually, shear, tensile, and piping discontinuities facilitate CO_2 leakage.

The dissolution of CO_2 and minerals in water increases the water density, and induces convective fluid circulation that sustains persistent coupled hydro-chemo-mechanical phenomena (Pruess and Zhang, 2008).

As water in the residual brine diffuses into supercritical CO_2, excess salts precipitate (e.g., calcite, halite, and anhydrate) and the formation absolute conductivity decreases (André et al., 2007; Kim, 2012 – Note: periodic fresh-water front prevents salt precipitation near the wellbore during the early stages of CO_2 injection). However, the relative permeability of CO_2 increases quite dramatically as the residual water saturation decreases, leading to a marked increase in injectivity.

5.3. Governing dimensionless ratios

Displacement patterns, efficiency, and storativity can be analyzed in terms of five dimensionless ratios (definitions in Table 1); for supercritical CO_2 storage, these ratios and salient implications follow (Note: listed ranges are based on typical values for parameters under reservoir conditions):

- Mobility number $10^{-1} < M < 10^{-2}$: susceptibility to viscous fingering (Lenormand et al., 1988).
- Capillary number $10^{-12} < C < 10^{-5}$ (for a flow rate 10^{-10} m/s $< q < 10^{-3}$ m/s): capillarity dominates over viscous drag when CO_2 invades water-filled porous media.
- Rayleigh number $4\pi^2 < \mathrm{Ra} < 10^4$ (for injection sites in the Alberta Basin – Hassanzadeh et al., 2007): convective instability is likely to emerge (Kneafsey and Pruess, 2010).
- Bond number $10^{-11} < B < 10^{-6}$ (for permeabilities 0.1 mD $< k <$ 10 D, density difference $\rho_w - \rho_{CO_2} = 400$ kg/m^3, and a CO_2–water interfacial tension $\gamma_{fl} = 35$ mN/m): compares the conditions for gravity-driven CO_2 advective flow during injection to capillarity.
- Trapping number Tr: compares the pressure difference between water and CO_2 in a pool of height H_{CO_2} to the capillary entry pressure in a reservoir rock with characteristic pore size R_{pore} in long-term conditions.

Experimental and numerical results presented above span the following zone of the dimensionless space: $M \approx 10^{-2.0}$–$10^{-0.4}$, $C \approx 10^{-8.0}$–$10^{-3.8}$ (Ra, B, and Tr are not available because no convection, gravity, and buoyancy is considered in experiments and numerical simulations in this study).

Surfactants lower the CO_2–water capillary factor $\gamma_{fl}\cdot\cos\theta$ below ~3 mN/m, and increase both the Bond number B and the Capillary number C by 1 or 2 orders of magnitude, which lead to larger CO_2 storage capacity (this study; see also Kopp et al., 2009). Viscous, capillary, and buoyant drives can be combined into a single dimensionless number Co to compare potential field situations:

$$Co = \frac{B \cdot M^{\alpha}}{C^{\beta}} \tag{11}$$

Higher oil recovery has been observed in drainage experiments when the combined number Co increases (Rostami et al., 2010).

5.4. 3D field conditions

Field conditions have higher pore connectivity and buoyant drive. Yet, the following arguments suggest that enhanced sweep efficiencies observed in our 2D studies are relevant to 3D field conditions.

Buoyant CO_2 pools rest against the seal layer and are laterally confined by either reservoir geometry and/or capillary trapping. Capillary trapping is pore size-dependent and inversely related to

Table 1
Dimensionless ratios in CO_2 invasion and geological storage.

Dimensionless ratio	Expression	Physical interpretation
Mobility number, M	$M = \frac{\mu_{CO_2}}{\mu_w}$	Ratio between CO_2 and water viscosities
Capillary number, C	$C = \frac{q\mu_{CO_2}}{\gamma_{fl}\cos\theta}$	Ratio between viscous and capillary forces
Rayleigh number, Ra	$\mathrm{Ra} = \frac{k\Delta\rho g H_{CO_2}}{\mu\phi D}$	Ratio between convection rate and diffusion rate
Bond number, B	$B = \frac{(\rho_w - \rho_{CO_2})gkk_{rCO_2}}{\gamma_{fl}\cos\theta}$	Ratio between conditions for gravity-driven CO_2 advective flow and for capillary phenomena (during injection)
Trapping number, Tr	$Tr = \frac{H_{CO_2}R_{pore}(\rho_w - \rho_{CO_2})g}{2\gamma_{fl}\cos\theta}$	Ratio between buoyant pressure to capillary trapping (long-term)

Note: CO_2 viscosity $\mu_{CO_2} = 4\times10^{-4}$ Pa s to 8×10^{-4} Pa s (Fenghour et al., 1998); water viscosity $\mu_w = 6\times10^{-3}$ Pa s to 8×10^{-3} Pa s (Adams and Bachu, 2002); q [m^3/s/m^2]: flow rate; γ_{fl} [N/m]: interfacial tension; θ [deg]: contact angle; ρ_i [kg/m^3]: the density of each phase; k [m^2]: permeability; k_{rCO_2} [–]: relative permeability of CO_2; D [m^2/s]: coefficient of molecular diffusion; H_{CO_2} [m]: CO_2 pool thickness.

injectivity. In the absence of geometric traps, the pool thickness H_{CO_2} can be estimated from equilibrium conditions (refer to Trapping number *Tr* in Table 1):

$$H_{CO_2} = \frac{2\gamma_{fl}\cos\theta}{R_{pore}(\rho_w - \rho_{CO_2})g} \quad (12)$$

Hence, reservoirs with adequate injectivity and no geometric traps will develop thin CO_2 pools with horizontal dimension much larger than the vertical dimension. Horizontal sweep efficiencies reported in this study clearly apply to such thin CO_2 pools in the field.

The Mobility *M* and Rayleigh Ra numbers are not affected by decreasing the capillary factor $\gamma_{fl}\cdot\cos\theta$. Yet, injection pressure and buoyancy have the same pore-scale implications at the time of invasion: in both cases, a reduction in the capillary factor $\gamma_{fl}\cdot\cos\theta$ enhances sweep efficiency by facilitating CO_2 invasion into smaller channels (for a given fluid pore velocity – refer to network simulation results in Section 4).

Finally, enhanced sweep efficiencies have been observed in vertical displacement experiments as the capillary number *C* increases (Suekane and Okada, 2013) or the combined *Co* number increases (Rostami et al., 2010).

6. Conclusions

We can engineer CO_2 injection to attain improved sweep efficiency. Possible alternatives include: increased CO_2 viscosity, sequential fluid injection, bio-clogging, and decreased capillary factor. In this study, we manipulated the capillary factor.

Surfactants that have hydrophilic heads and CO_2-philic tails lower the interfacial tension between CO_2 and water. The long-chain nonionic surfactant used in these experiments (weight percent $wt \approx 0.4\%$) lowered the CO_2–water interfacial tension from $\gamma_{fl} \sim 50$ mN/m to $\gamma_{fl} \sim 4$ mN/m at a pressure of $P \geq 7$ MPa. The parallelism in surface tension-*vs*-pressure trends for tests conducted with and without surfactant suggests a pressure-independent concentration of surfactants at the interface.

The contact angle formed by a water-surfactant droplet resting on a glass substrate and surrounded by CO_2 increases from $\theta \sim 20^\circ$ at $P = 0.1$ MPa to $\theta \sim 70^\circ$ at $P = 10$ MPa. Reduced interfacial tension γ_{fl} and larger contact angle θ combine to produce a marked decrease in the capillary factor $\gamma_{fl}\cdot\cos\theta$.

Young's equation $\gamma_{fl}\cdot\cos\theta = \gamma_{fs} - \gamma_{ls}$ implies that pressure and surfactants also affect the balance between mineral–CO_2 γ_{fs} and water–mineral γ_{ls} interfacial tensions.

Experimental CO_2 injection tests in pore micro-models and parallel network model simulations demonstrate that the sweep efficiency of CO_2 invasion can be effectively enhanced by lowering the capillary factor $\gamma_{fl}\cdot\cos\theta$. In particular, the sweep efficiency can double with the addition of surfactants.

Engineered CO_2 injection such as using surfactants can optimize pore space occupancy underground and minimize emergent hydro-chemo-mechanically coupled phenomena such as salt precipitation near the well (lower injection difficulties), water acidification and mineral dissolution (lower possibility of piping, internal shear, and differential settlement), and long-term convective flow. Consequently, improved long-term integrity of storage reservoirs is anticipated.

Surfactant cost – aggravated by sorption – may offset the technical advantages identified in this study. However, there are adequate surfactants commercially available today, and active research to develop enhanced low-cost CO_2-soluble nonionic surfactants.

Acknowledgements

Support for this research was provided by the U.S. Department of Energy project DE-FE0001826 with additional funding by The Goizueta Foundation. HUNTSMAN donated the surfactant SURFONIC POA-25R2. F.J. Santamarina and E. Papadopoulos carefully edited this manuscript. We are grateful to insightful comments by the anonymous reviewers. Any opinion, findings, conclusions, or recommendations expressed herein are those of the authors and do not necessarily reflect the views of funding organizations.

References

Adams, J., Bachu, S., 2002. Equations of state for basin geofluids: algorithm review and intercomparison for brines. Geofluids 2, 257–271.
Aker, E., JØrgen MÅlØy, K., Hansen, A., Batrouni, G., 1998. A two-dimensional network simulator for two-phase flow in porous media. Transport in Porous Media 32, 163–186.
Alvarado, V., Manrique, E., 2010. Enhanced oil recovery: an update review. Energies 3, 1529–1575.
André, L., Audigane, P., Azaroual, M., Menjoz, A., 2007. Numerical modeling of fluid–rock chemical interactions at the supercritical CO_2–liquid interface during CO_2 injection into a carbonate reservoir, the Dogger aquifer (Paris Basin, France). Energy Conversion and Management 48, 1782–1797.
Bachu, S., Bennion, B., 2008. Effects of in-situ conditions on relative permeability characteristics of CO_2-brine systems. Environmental Geology 54, 1707–1722.
Baines, S.J., Worden, R.H., 2004. The long-term fate of CO_2 in the subsurface: natural analogues for CO_2 storage. Geological Society, London, Special Publications 233, 59–85.
Bryant, S., Britton, L., 2008. Mechanistic Understanding of Microbial Plugging for Improved Sweep Efficiency. US DOE NETL Report DE-FC26-04NT15524.
Bryant, S.L., Lakshminarasimhan, S., Pope, G.A., 2008. Buoyancy-dominated multiphase flow and its effect on geological sequestration of CO_2. SPE Journal 13, 447–454.
Cha, M.S., 2012. Consequences of mineral dissolution in sediments. Civil and Environmental Engineering, Georgia Institute of Technology, Atlanta, GA.
Chalbaud, C., Robin, M., Lombard, J.M., Martin, F., Egermann, P., Bertin, H., 2009. Interfacial tension measurements and wettability evaluation for geological CO_2 storage. Advances in Water Resources 32, 98–109.
Chun, B.-S., Wilkinson, G.T., 1995. Interfacial tension in high-pressure carbon dioxide mixtures. Industrial & Engineering Chemistry Research 34, 4371–4377.
da Rocha, S.R.P., Harrison, K.L., Johnston, K.P., 1999. Effect of surfactants on the interfacial tension and emulsion formation between water and carbon dioxide. Langmuir 15, 419–428.
De Gennes, P.G., Brochard-Wyart, F., Quéré, D., 2004. Capillarity and Wetting Phenomena: Drops, Bubbles, Pearls, Waves. Springer Verlag.
Dickson, J.L., Gupta, G., Horozov, T.S., Binks, B.P., Johnston, K.P., 2006. Wetting phenomena at the CO_2/water/glass interface. Langmuir 22, 2161–2170.
Dickson, J.L., Smith Jr., P.G., Dhanuka, V.V., Srinivasan, V., Stone, M.T., Rossky, P.J., Behles, J.A., Keiper, J.S., Xu, B., Johnson, C., 2005. Interfacial properties of fluorocarbon and hydrocarbon phosphate surfactants at the water–CO_2 interface. Industrial & Engineering Chemistry Research 44, 1370–1380.
Dooley, J.J., Dahowski, R.T., Davidson, C.L., Wise, M.A., Gupta, N., Kim, S.H., Malone, E.L., 2006. Carbon Dioxide Capture and Geologic Storage: A Core Element of a Global Energy Technology Strategy to Address Climate Change. A Technology Report from the Second Phase of the Global Energy Technology Strategy Program.
Duan, Z., Sun, R., 2003. An improved model calculating CO_2 solubility in pure water and aqueous NaCl solutions from 273 to 533 K and from 0 to 2000 bar. Chemical Geology 193, 257–271.
EIA, U., 2004. The Basics of Underground Natural Gas Storage.
EIA, U., 2010. In: Newell, R. (Ed.), Annual Energy Outlook 2011: Reference Case. EIA, U., Washington, DC.
Enick, R.M., Ammer, J., 1998. A Literature Review of Attempts to Increase the Viscosity of Dense Carbon Dioxide. US DOE NETL Report DE-AP26-97FT25356.
Enick, R.M., Beckman, E.J., Johnson, J.K., Hamilton, A., 2010. Synthesis and Evaluation of CO_2 Thickeners Designed with Molecular Modeling, DE-FG26-04NT-15533. University of Pittsburgh.
Enick, R.M., Olson, D.K., 2012. Mobility and Conformance Control for Carbon Dioxide Enhanced Oil Recovery (CO2-EOR) via Thickeners, Foams and Gels – A Detailed Literature Review of 40 Years of Research. DOE/NETL-2012/1540.
Espinoza, D.N., Kim, S.H., Santamarina, J.C., 2011. CO_2 geological storage—geotechnical implications. KSCE Journal of Civil Engineering 15, 707–719.
Espinoza, D.N., Santamarina, J.C., 2010. Water–CO_2–mineral systems: Interfacial tension, contact angle, and diffusion—implications to CO_2 geological storage. Water Resources Research 46, W07537.
Farajzadeh, R., Andrianov, A., Bruining, H., Zitha, P.L., 2009. Comparative study of CO_2 and N_2 foams in porous media at low and high pressure–temperatures. Industrial & Engineering Chemistry Research 48, 4542–4552.
Fenghour, A., Wakeham, W.A., Vesovic, V., 1998. The viscosity of carbon dioxide. Journal of Physical and Chemical Reference Data 27, 31–44.

Fenwick, D., Blunt, M., 1998. Three-dimensional modeling of three phase imbibition and drainage. Advances in Water Resources 21, 121–143.
Ferer, M., Bromhal, G.S., Smith, D.H., 2003. Pore-level modeling of immiscible drainage: validation in the invasion percolation and DLA limits. Physica A: Statistical Mechanics and its Applications 319, 11–35.
Francisca, F., Fratta, D., Wang, H., 2008. Electrowetting on mineral and rock surfaces. Geophysical Research Letters 35, L06402.
Fredd, C.N., Fogler, H.S., 1998. Influence of transport and reaction on wormhole formation in porous media. AIChE Journal 44, 1933–1949.
Gresham, R.L., McCoy, S.T., Apt, J., Morgan, M.G., 2010. Implications of compensating property owners for geologic sequestration of CO_2. Environmental Science & Technology 44, 2897–2903.
Hassanzadeh, H., Pooladi-Darvish, M., Keith, D.W., 2007. Scaling behavior of convective mixing, with application to geological storage of CO_2. AIChE Journal 53, 1121–1131.
Huh, C., Rossen, W., 2008. Approximate pore-level modeling for apparent viscosity of polymer-enhanced foam in porous media. SPE Journal 13, 17–25.
IPCC, 2005. IPCC special report on carbon dioxide capture and storage. In: Metz, B., Davidson, O., de Coninck, H.C., Loos, M., Meyer, L.A. (Eds.), Prepared by Working Group III of the Intergovernmental Panel on Climate Change. Cambridge University Press, Cambridge, UK/New York, USA, p. 442.
Jang, J., 2011. Gas Production from Hydrate-Bearing Sediments. Civil and Environmental Engineering, Georgia Institute of Technology, Atlanta, GA.
Kam, S.I., Rossen, W.R., 2003. A model for foam generation in homogeneous media. SPE Journal 8, 417–425.
Kharaka, Y.K., Cole, D.R., Hovorka, S.D., Gunter, W.D., Knauss, K.G., Freifeld, B.M., 2006. Gas–water–rock interactions in Frio formation following CO_2 injection: implications for the storage of greenhouse gases in sedimentary basins. Geology 34, 577–580.
Kim, S.H., 2012. CO_2 Geological Storage: Hydro-Chemo-Mechanically Coupled Phenomena and Engineered Injection. Civil and Environmental Engineering, Georgia Institute of Technology, Atlanta, GA, pp. 188.
Kinart, C.M., Kinart, W.J., Cwiklinska, A., 2002. Density and viscosity at various temperatures for 2-methoxyethanol + acetone mixtures. Journal of Chemical & Engineering Data 47, 76–78.
Kneafsey, T.J., Pruess, K., 2010. Laboratory flow experiments for visualizing carbon dioxide-induced, density-driven brine convection. Transport in Porous Media 82, 123–139.
Kopp, A., Class, H., Helmig, R., 2009. Investigations on CO_2 storage capacity in saline aquifers: part 1. Dimensional analysis of flow processes and reservoir characteristics. International Journal of Greenhouse Gas Control 3, 263–276.
Kovscek, A.R., Bertin, H.J., 2003. Foam mobility in heterogeneous porous media. Transport in Porous Media 52, 17–35.
Kozlov, M.Y., Melik-Nubarov, N.S., Batrakova, E.V., Kabanov, A.V., 2000. Relationship between pluronic block copolymer structure, critical micellization concentration and partitioning coefficients of low molecular mass solutes. Macromolecules 33, 3305–3313.
Kvamme, B., Kuznetsova, T., Hebach, A., Oberhof, A., Lunde, E., 2007. Measurements and modelling of interfacial tension for water plus carbon dioxide systems at elevated pressures. Computational Materials Science 38, 506–513.
Lake, L.W., Venuto, P.B., 1990. A niche for enhanced oil recovery in the 1990s. Oil & Gas Journal 88, 62–67.
Lenormand, R., Touboul, E., Zarcone, C., 1988. Numerical models and experiments on immiscible displacements in porous media. Journal of Fluid Mechanics 189, 165–187.
Levitt, D., Jackson, A., Heinson, C., Britton, L., Malik, T., Dwarakanath, V., Pope, G., 2009. Identification and evaluation of high-performance EOR surfactants. SPE Reservoir Evaluation & Engineering 12, 243–253.
Liu, K., Kiran, E., 2007. Viscosity, density and excess volume of acetone + carbon dioxide mixtures at high pressures. Industrial & Engineering Chemistry Research 46, 5453–5462.
Massoudi, R., King, A.D., 1975. Effect of pressure on surface-tension of aqueous-solutions – adsorption of hydrocarbon gases, carbon-dioxide, and nitrous-oxide on aqueous-solutions of sodium-chloride and tetra-normal-butylammonium bromide at 25 degrees. Journal of Physical Chemistry 79, 1670–1675.
NETL, M., 2010. Carbon Sequestration Atlas of the United States and Canada. US Department of Energy, Office of Fossil Energy, National Energy Technology Laboratory.
Okwen, R.T., Stewart, M.T., Cunningham, J.A., 2010. Analytical solution for estimating storage efficiency of geologic sequestration of CO_2. International Journal of Greenhouse Gas Control 4, 102–107.
Pasten, C., Santamarina, J.C., 2012. Energy and quality of life. Energy Policy 49, 468–476.
Pečar, D., Doleček, V., 2005. Volumetric properties of ethanol–water mixtures under high temperatures and pressures. Fluid Phase Equilibria 230, 36–44.
Phadnis, H.S., Santamarina, J.C., 2011. Bacteria in sediments: pore size effects. Geotechnique Letters 1, 91–93.
Phillips, A.J., Lauchnor, E., Eldring, J., Esposito, R., Mitchell, A.C., Gerlach, R., Cunningham, A.B., Spangler, L.H., 2012. Potential CO_2 leakage reduction through biofilm-induced calcium carbonate precipitation. Environmental Science & Technology 47, 142–149.
Prasad, K.N., Luong, T.T., FlorenceJoelle Paris, A.T., Vaution, C., Seiller, M., Puisieux, F., 1979. Surface activity and association of ABA polyoxyethylene–polyoxypropylene block copolymers in aqueous solution. Journal of Colloid and Interface Science 69, 225–232.
Pruess, K., Zhang, K., 2008. Numerical Modeling Studies of the Dissolution-Diffusion-Convection Process During CO_2 Storage in Saline Aquifers. Lawrence Berkeley National Laboratory.
Pusch, G., Ionescu, G.F., May, F., Voigtländer, G., Stecken, L., Vosteen, H.D., 2010. Common features of carbon dioxide and underground gas storage (1). Oil Gas: European Magazine 36, 131–137.
Rebata-Landa, V., Santamarina, J.C., 2006. Mechanical limits to microbial activity in deep sediments. Geochemistry Geophysics Geosystems 7, Q11006.
Rebata-Landa, V., Santamarina, J.C., 2012. Mechanical Effects of Biogenic Nitrogen Gas Bubbles in Soils. Journal of Geotechnical and Geoenvironmental Engineering 138, 128–137.
Rostami, B., Kharrat, R., Pooladi-Darvish, M., Ghotbi, C., 2010. Identification of fluid dynamics in forced gravity drainage using dimensionless groups. Transport in Porous Media 83, 725–740.
Rotenberg, Y., Boruvka, L., Neumann, A., 1983. Determination of surface tension and contact angle from the shapes of axisymmetric fluid interfaces. Journal of Colloid and Interface Science 93, 169–183.
Ryoo, W., Webber, S.E., Johnston, K.P., 2003. Water-in-carbon dioxide microemulsions with methylated branched hydrocarbon surfactants. Industrial & Engineering Chemistry Research 42, 6348–6358.
Shin, H., Santamarina, J.C., 2009. Mineral dissolution and the evolution of k_0. Journal of Geotechnical and Geoenvironmental Engineering 135, 1141–1147.
Shin, H., Santamarina, J.C., Cartwright, J.A., 2010. Displacement field in contraction-driven faults. Journal of Geophysical Research 115, B07408.
Stone, M.T., Smith Jr., P.G., da Rocha, S.R.P., Rossky, P.J., Johnston, K.P., 2004. Low interfacial free volume of stubby surfactants stabilizes water-in-carbon dioxide microemulsions. Journal of Physical Chemistry B 108, 1962–1966.
Suekane, T., Soukawa, S., Iwatani, S., Tsushima, S., Hirai, S., 2005. Behavior of supercritical CO_2 injected into porous media containing water. Energy 30, 2370–2382.
Suekane, T., Okada, K., 2013. Gas injection in a water saturated porous medium: Effect of capillarity, buoyancy, and viscosity ratio. Energy Procedia 37, 5545–5552.
Sutjiadi-Sia, Y., Jaeger, P., Eggers, R., 2008. Interfacial tension of solid materials against dense carbon dioxide. Journal of Colloid and Interface Science 320, 268–274.
Sutjiadi-Sia, Y., Marckmann, H., Eggers, R., Holzknecht, C., Kabelac, S., 2007. The effect of in liquids dissolved dense gases on interfacial and wetting characteristics. Forschung Im Ingenieurwesen-Engineering Research 71, 29–45.
Szymczyk, K., Jańczuk, B., 2008. Wettability of a glass surface in the presence of two nonionic surfactant mixtures. Langmuir 24, 7755–7760.
Tanaka, Y., Matsuda, Y., Fujiwara, H., Kubota, H., Makita, T., 1987. Viscosity of (water + alcohol) mixtures under high pressure. International journal of thermophysics 8, 147–163.
Tsouris, C., Aaron, D.S., Williams, K.A., 2010. Is carbon capture and storage really needed? Environmental Science & Technology 44, 4042–4045.